

Temperature-Dependent Far-Infrared Spectra of Single Crystals of High Explosives Using Terahertz Time-Domain Spectroscopy

Jeffrey Barber, Daniel E. Hooks, and David J. Funk*

DX Division, Los Alamos National Laboratory, Los Alamos, New Mexico 87545

Richard D. Averitt and Antoinette J. Taylor

MST Division, Los Alamos National Laboratory, Los Alamos, New Mexico 87545

Dmitri Babikov

Chemistry Department, Marquette University, Milwaukee, Wisconsin 53201

Received: December 9, 2004; In Final Form: February 21, 2005

Survey spectra of single-crystal HMX (octahydro-1,3,5,7-tetranitro-1,3,5,7-tetrazocine), RDX (hexahydro-1,3,5-trinitro-1,3,5-triazine), and PETN (pentaerythritol tetranitrate) were acquired in the region from 10 to 80 cm^{-1} using terahertz time-domain spectroscopy. The spectra were taken at temperatures ranging from 8.4 to 300 K. Generally, the spectra show multiple absorption peaks in the range 50–80 cm^{-1} , with PETN (110) showing strong absorption features at room temperature. RDX (210) is the most notable in the region 10–40 cm^{-1} , showing multiple spectral features, while HMX (010) shows a very broad absorption at 47.8 cm^{-1} with a fwhm of 37.3 cm^{-1} . Future plans include polarization-dependent investigations for multiple crystallographic orientations over an increased spectral range and higher-level theoretical calculations.

I. Introduction

THz time-domain spectroscopy (THz-TDS) has recently gained significant attention for its potential use as a noninvasive diagnostic.¹ Applications include medical imaging, process monitoring, and long wave machine vision control. In addition, THz-TDS has been looked upon as a potential candidate for a real-time drug or explosive detection instrument that would be benign to human subjects. However, the spectra of many of these materials are not known in the 10–100 cm^{-1} spectral region. To remedy this deficiency, we have initiated a systematic study of energetic material absorptions in this long-wavelength spectral regime. In addition to cataloguing the spectra for detection purposes, our studies will provide some information regarding the density of “doorway” states, that is, those states that may provide facile energy transfer into the molecular framework via anharmonic coupling to phonon modes of the lattice when the energetic material is shock-loaded.

II. Experimental Section

The THz-TDS measurements were performed using a 1 kHz regeneratively amplified Ti:sapphire laser producing 50 fs pulses at 800 nm. A portion of the amplifier output was used to generate THz pulses in (110) oriented ZnTe through optical rectification. Following transmission through the cryostat/sample, the transmitted THz pulses were measured using the Pockels effect in (110) ZnTe. For both the emitter and the detector, 1 mm thick (110) ZnTe crystals bonded to 2 mm thick (100) were employed. By bonding the electrooptically active (110) crystals to the inactive (100) crystals, a broad THz bandwidth is preserved while pushing etalons in the crystals to longer time. This allows for higher resolution to be obtained in an electrooptic THz-TDS system. The entire THz path was

purged with nitrogen to minimize water vapor absorption, and a continuous-flow helium cryostat was used for the temperature-dependent measurements. The thickness and orientation of the crystals used in this study are presented in Table 1 along with the spectral resolution.

HE samples were cut from large single crystals. UK manufactured HMX and RDX was dried, purified by Soxhlet extraction in acetone, and recrystallized in acetone prior to use. HMX crystals were grown by slow evaporation of acetone at 32°C, in a 1000 mL, tall, spoutless beaker covered by a Parafilm coated watch glass. The bottom one-third of the beaker was immersed in the heating bath, and the top was open to air at room temperature. This method allowed for convective mixing, and the reflux continuously washed the beaker sides, preventing parasitic growth. Seeds grown from cooled dimethyl sulfoxide, typically 100 mg each, were dropped into the solution when the proper level of saturation was achieved. Crystals were harvested after 3 or 4 weeks of growth. The same general technique was used to grow RDX and PETN crystals, with the exception that ethyl acetate was the growth solvent in the case of PETN. The exact details of crystal growth of RDX and PETN, and the pedigree of the PETN starting material, are not known as these crystals were chosen from a stock grown by Howard Cady several years ago.² Crystals chosen to cut samples from were greater than 8 g in all cases and were optically clear. Contact goniometry was used to locate planes by redundant reference to crystal facets, which were then cut using a low-speed (cut rate ~ 0.5 cm/h) diamond-impregnated wire saw, using a solution of Alconox in deionized water as a lubricant. The surfaces of the crystals were hand-polished to thickness using optical-grade 9 μm abrasive paper with the same lubricant. The final orientation of each surface was verified by transmission Laue X-ray diffraction to be within one-half degree of the desired faces. Plane indices are given with respect to the $P4_21c$ (PETN), $Pbca$ (RDX), and $P2_1/n$ (β -HMX) space groups.

* Corresponding author. E-mail: djf@lanl.gov.

TABLE 1: Experimental Parameters

sample	orientation	thickness (mm)	resolution (cm ⁻¹)
PETN	(101)	1.09	1.4
	(110)	0.83	1.4
RDX	(210)	0.94	1.4
	(111)	0.84	1.4
	(100)	1.03	1.4
HMX	(011)	1.52	1.3
	(110)	2.05	1.3
	(010)	1.02	1.7

III. Computational Methods

All calculations were carried out using the Gaussian 03 software package.³ The B3LYP method was used in conjunction with the 6-31G* basis set. Starting with the structures obtained from experimental X-ray crystallographic data,^{4–6} gas-phase single-molecule geometry optimizations and frequency calculations were performed. This method was similar to the method used by Brand and co-workers, with present calculations including the addition of *Int=Ultrafine* and *Opt=Tight*.⁷ These keywords were added due to our interest in low-frequency modes. Calculations were performed on an IBM SP RS/6000 16-processor node of the Seaborg supercomputer at the National Energy Research Scientific Computing Center at Lawrence Berkeley National Laboratory.

IV. Analysis

To extract the complex conductivity or complex index from the THz-TDS data, the method detailed in the paper by Duvillaret et al. was used.⁸ Briefly, time-domain data are acquired with and without the sample in the beam path. Figure 1 shows representative time-domain data for this experiment. The data are fast Fourier transformed (FFT), and the ratio of the sample data to the reference data is taken to yield the complex transmission coefficient as a function of frequency, $T(\omega)$, eliminating the need for the use of Kramers–Kronig relations.⁹ In the data acquired here, the samples are treated as optically thick, simplifying the analysis by eliminating the need to account for “multiple reflections” caused by the air–sample boundaries.⁸ Small ripples in the spectra are indicative of a reflection that is not accounted for in the analysis. Truncating the data prior to the reflection smooths the data, but also decreases the spectral resolution. As noted in ref 8, forming the following error function yields a surface having the approximate form of a paraboloid:

$$\delta(n_2, k_2) = \delta\rho^2 + \delta\phi^2 \quad (1)$$

where

$$\delta\rho = \ln(|T(\omega)|) - \ln(|T_{\text{meas}}(\omega)|) \quad (2)$$

and

$$\delta\phi = \arg(T(\omega)) - \arg(T_{\text{meas}}(\omega)) \quad (3)$$

where $T(\omega)$ is the calculated and $T_{\text{meas}}(\omega)$ is the measured complex transmission coefficient. Initial values are generated for the complex index (n_2, k_2) of the sample, and the error function is minimized using a standard algorithm (optimize function in Igor Pro, Wavemetrics Corp.). This yields values for n_2 and k_2 as a function of frequency, which is the desired result. As a check, an estimate of the frequency dependence of the absorption coefficient of each sample was made using a

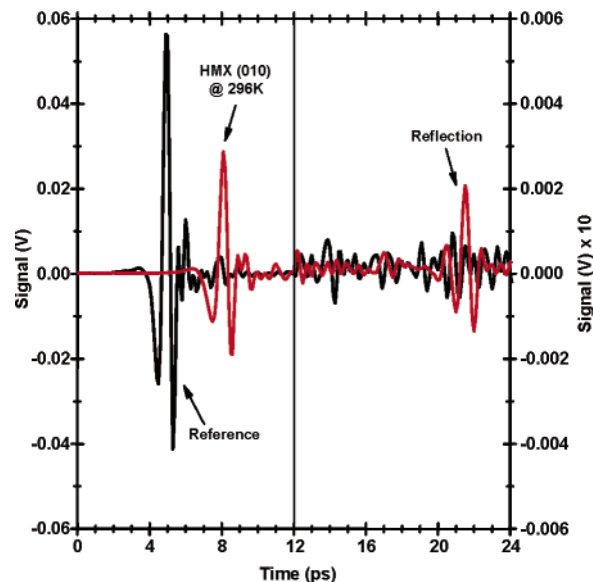


Figure 1. Typical time-domain data for this work. The right panel has been expanded by a factor of 10 to show detail in the signal, including a reflection internal to the crystal.

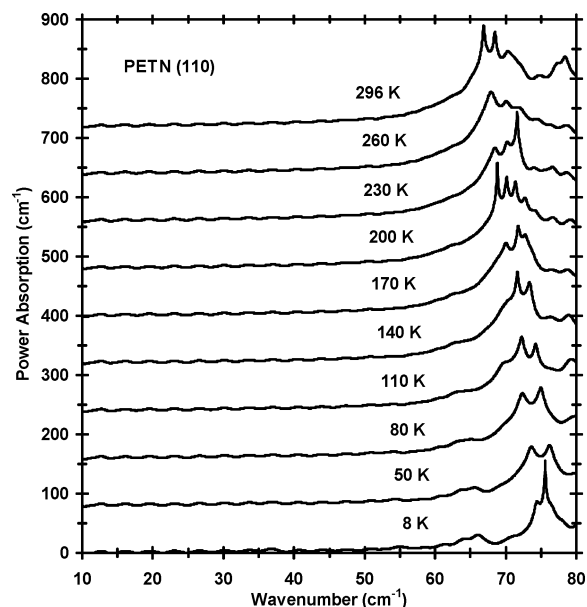


Figure 2. Far-infrared absorption spectra of PETN (110) from 8 to 296 K.

simple Beer’s Law analysis (neglecting Fresnel losses at the interfaces) and was found to agree with the absorption coefficients obtained by the rigorous technique described above. Finally, we note, and as pointed out in ref 8, the phase delay between the sample and reference is only determined to modulo 2π ; therefore, care must be taken to accurately determine the index. Thus, for each sample, we use the peak temporal delay to determine the coefficient m , the number of 2π wraps that are undetermined by the FFT, and then used the analysis described above to determine (n_2, k_2) . In the following, we only present the data for the power absorption (in all figures, the curves are displaced vertically for clarity).

V. Results and Discussion

Figures 2 and 3 show the absorption spectra for PETN (110) and (101), respectively. The temperature range is from 8 to 296 K. It can be seen that the spectra of these two orientations are

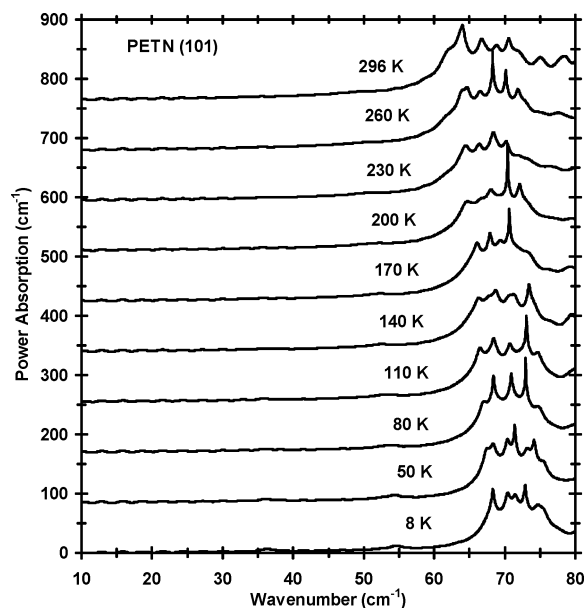


Figure 3. Far-infrared absorption spectra of PETN (101) from 8 to 296 K.

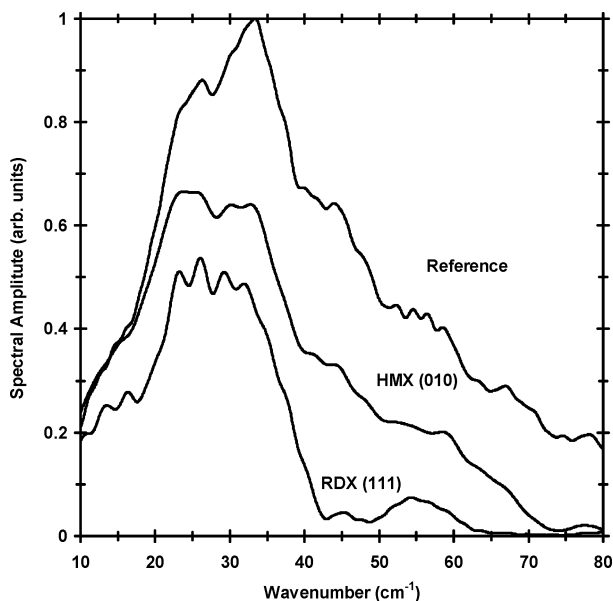


Figure 4. Typical spectral amplitudes seen in the range 10–80 cm^{-1} .

similar below 60 cm^{-1} , with little real structure being present. In the (101) data, weak absorption peaks at 37 and 55 cm^{-1} appear as the temperature is decreased. Above 60 cm^{-1} , PETN (101) has more spectral features present, as emphasized in the 8 K spectrum. Of note are the strong absorption peaks for the PETN (110) sample. Many of the peaks disappear at low temperatures, leaving a large peak centered at 75.6 cm^{-1} , indicating that the structures at higher temperatures are most likely hot bands.

Figure 4 shows examples of the terahertz signals generated in this work. A typical reference signal (no sample in beam) for this work is shown and is consistent with Figure 2A of ref 10. Also included are the terahertz signals with HMX (010) and RDX (111) samples. The reader should take some caution with results at the upper and lower ends of the absorption spectra presented here. These are the regions of our terahertz envelope where our signal levels are weaker. In addition, some samples are strong absorbers in these regions, which could lead to potential problems with the accuracy of the spectra. For example,

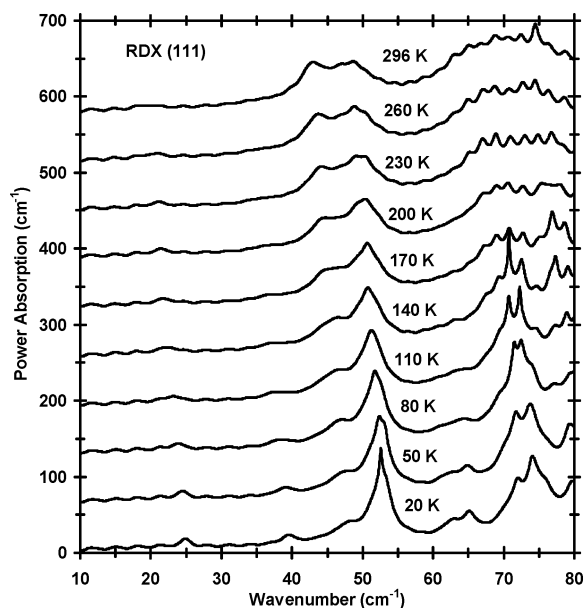


Figure 5. Far-infrared absorption spectra of RDX (111) from 20 to 296 K.

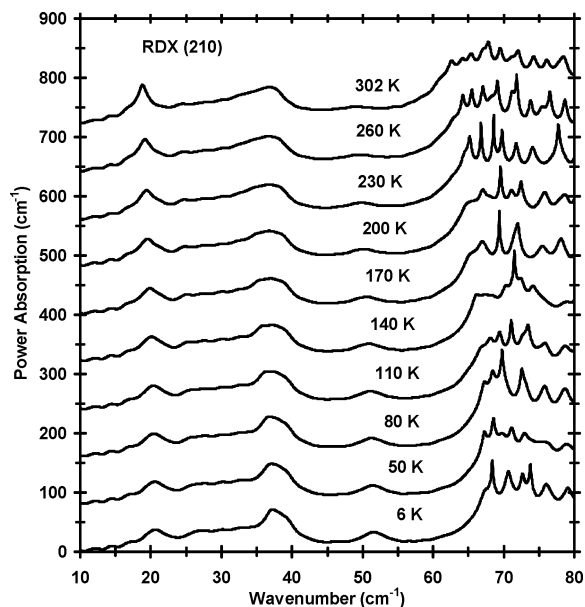


Figure 6. Far-infrared absorption spectra of RDX (210) from 6 to 302 K.

the terahertz signal for RDX (111) is shown in Figure 4 as an illustration as it is a nearly complete absorber above 65 cm^{-1} . The absorption spectra for RDX (111), shown in Figure 5, have a number of peaks above 65 cm^{-1} , which sharpen and broaden as temperature changes. While there are clearly absorption peaks present, the shapes of these peaks are not absolutely determined. In attempting to analyze line shapes in the region where our terahertz signals are stronger, it was found that the absorptions could not be fit with a standard line-shape profile such as a Lorentzian function. This is most likely due to the complex nature of the spectrum and overlapped modes that are not resolved in this study.

Three crystal orientations of RDX were studied, (111), (210), and (100), shown in Figures 5–7. The most prominent feature for RDX (111) is the strong absorption at 52.6 cm^{-1} . This feature increases in magnitude and sharpens with decreasing temperature. In contrast, the magnitude of the shoulder present at 47.3 cm^{-1} gradually decreases with decreasing temperature,

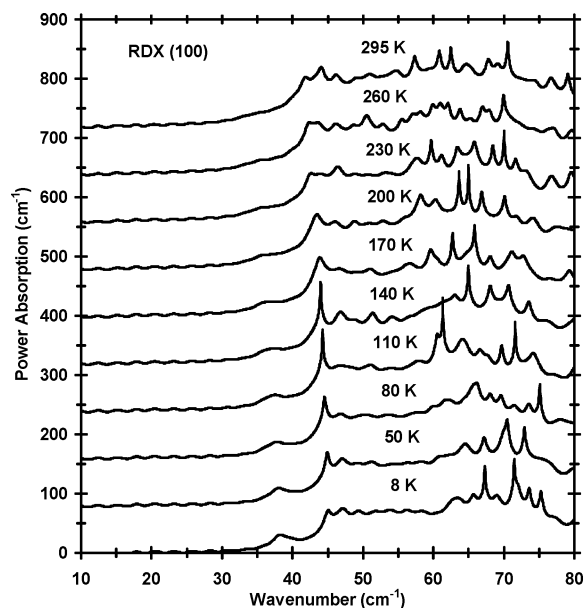


Figure 7. Far-infrared absorption spectra of RDX (100) from 8 to 295 K.

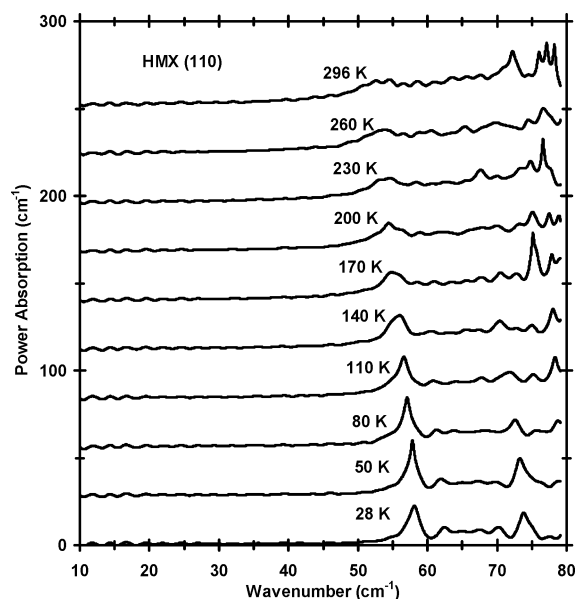


Figure 9. Far-infrared absorption spectra of HMX (110) from 28 to 296 K.

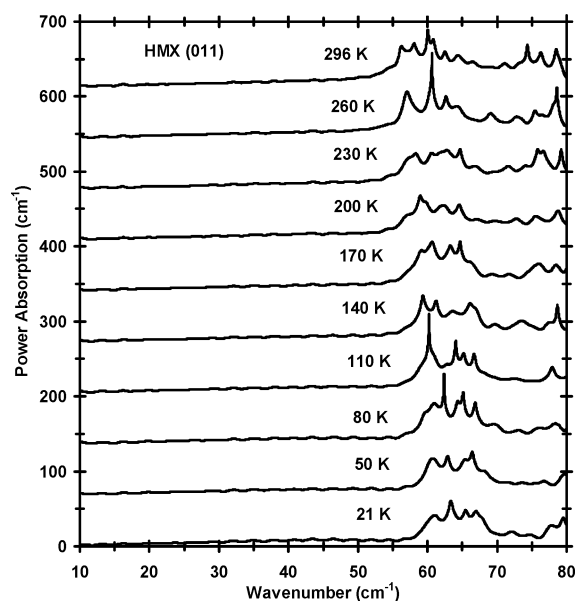


Figure 8. Far-infrared absorption spectra of HMX (011) from 21 to 296 K.

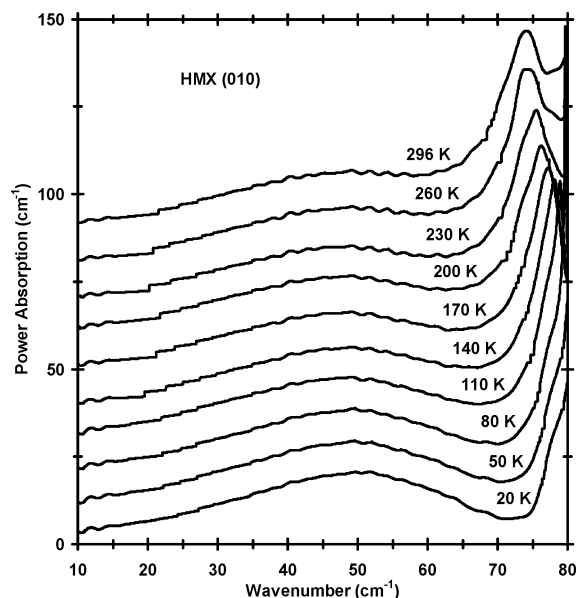


Figure 10. Far-infrared absorption spectra of HMX (010) from 20 to 296 K.

suggesting that the appropriate assignment is a hot band of the vibration at 52.6 cm^{-1} . For the region from 10 to 40 cm^{-1} , RDX (210) exhibits the strongest absorption. With decreasing temperature, the amplitude of the absorption peak centered near 38 cm^{-1} increases. This peak is asymmetric in shape at all temperatures, indicating the presence of more than one vibration. RDX (100) absorption peaks begin to grow in near 40 cm^{-1} , and all temperatures demonstrate a complex structure that is not spectrally resolved in the present studies. Multiple closely spaced peaks are present, causing different peaks to maximize at various temperatures as the populations in higher vibrational states diminish. Similarly, the absorption spectra for RDX (210) and (111) above 55 cm^{-1} reveal a large number of peaks contributing to the complicated overall structure for these crystals at all temperatures.

Figures 8–10 show the spectra for HMX (011), (110), and (010), respectively. HMX (011) and (110) are similar in that most of the absorption peaks lie above 50 cm^{-1} . For (110),

absorption peaks grow in at 58 and 74 cm^{-1} as temperature decreases. The (011) orientation shows a much more complicated spectrum at low temperature with several peaks present. It should be noted that HMX is not as strong an absorber in this region as the other explosive crystals. Probably the most curious aspect of all of the spectra presented in this work is that of HMX (010). This sample shows little complex structure in the region studied, but does show a very broad absorption feature that is not observed in the other samples. Fitting this peak to a Lorentzian profile yields an optimum center position of 47.8 cm^{-1} and a fwhm of 37.3 cm^{-1} . The spectral resolution for this sample was reduced to prevent the rippling effect due to the internal reflection in the sample (seen in Figure 1) from obscuring this feature. It is hoped that future theoretical calculations will elucidate the nature of the results for this orientation.

In comparing results, the differences between experimental studies on single crystals and theoretical calculations on gas-phase molecules should be mentioned. Clearly, calculated phonon modes are not available through the methods used for

TABLE 2: Structural Parameters for RDX

Bond Length (Å)					
parameter	experiment ^a	calculated ^b	parameter	experiment	calculated
C1–N1	1.464(4)	1.47344	C3–H6	1.075(9)	1.08408
C1–N2	1.443(4)	1.44901	N1–N4	1.351(3)	1.40216
C2–N2	1.468(4)	1.46210	N2–N5	1.392(3)	1.43175
C2–N3	1.458(4)	1.46207	N3–N6	1.398(3)	1.43161
C3–N3	1.440(4)	1.44899	N4–O1	1.209(5)	1.22576
C3–N1	1.450(4)	1.47345	N4–O2	1.233(4)	1.22576
C1–H1	1.058(10)	1.09943	N5–O3	1.203(5)	1.22016
C1–H2	1.092(8)	1.08407	N5–O4	1.207(5)	1.22115
C2–H3	1.085(8)	1.08511	N6–O5	1.201(5)	1.22016
C2–H4	1.087(7)	1.09379	N6–O6	1.205(5)	1.22117
C3–H5	1.088(8)	1.09944			
Bond Angle (deg)					
parameter	experiment ^a	calculated ^b	parameter	experiment	calculated
N1–C1–N2	107.8(2)	109.266	C3–N1–C1	115.1(2)	115.024
N1–C1–H1	109.9(4)	110.903	C3–N1–N4	120.9(2)	115.069
N1–C1–H2	110.0(4)	109.379	C1–N1–N4	119.7(2)	115.068
N2–C1–H1	108.0(4)	107.547	N1–N4–O1	117.2(3)	116.600
N2–C1–H2	110.0(5)	109.950	N1–N4–O2	117.8(3)	116.602
H1–C1–H2	111.0(6)	109.773	O1–N4–O2	125.0(3)	126.775
N2–C2–N3	111.7(2)	112.706	C1–N2–C2	114.6(2)	115.457
N2–C2–H3	110.1(4)	109.772	C1–N2–N5	117.1(2)	116.041
N2–C2–H4	106.9(4)	107.211	C2–N2–N5	116.6(2)	116.501
N3–C2–H3	110.7(4)	109.766	N2–N5–O3	117.2(3)	116.112
N3–C2–H4	107.2(4)	107.222	N2–N5–O4	116.8(3)	116.630
H3–C2–H4	110.1(6)	110.090	O3–N5–O4	125.7(4)	127.108
N3–C3–N1	108.4(2)	109.269	C2–N3–C3	114.8(2)	115.480
N3–C3–H5	107.4(4)	107.557	C2–N3–N6	117.5(2)	116.521
N3–C3–H6	111.1(4)	109.942	C3–N3–N6	115.6(2)	116.064
N1–C3–H5	109.6(4)	110.901	N3–N6–O5	117.3(3)	116.112
N1–C3–H6	111.3(5)	109.378	N3–N6–O6	117.0(3)	116.633
H5–C3–H6	108.8(6)	109.771	O5–N6–O6	125.5(4)	127.105

^a Reference 4. ^b B3LYP/6-31G*.

this work. Rigorous theoretical study of crystalline molecular solids requires performing calculations for the system of molecules in the unit cell with periodic boundary conditions.¹¹ This is a difficult task computationally, particularly in the case of RDX where the unit cell contains 8 H₃C₃N₆O₆ molecules. Furthermore, the vibrational analysis for density functional theory calculations with periodic boundary conditions has not been implemented into current quantum chemistry calculations. However, our computational results provide insight into the spectra presented here by attempting to positively identify those modes that are intramolecular in nature. It should be noted here that there were convergence problems with the addition of *Opt=Tight* and *Int=Ultrafine* keywords to our calculations. For RDX, it was found that there was no significant difference from calculations without these additions. For this reason, we chose to use the B3LYP/6-31G* results for RDX without our additional criteria and use the results from Brand et al. (HMX) and Gruzdkov and Gupta (PETN) such that a comparison could be made on a consistent basis.^{7,12}

Tables 2 and 3 contain the ab initio results for the molecules studied here. As in the case of refs 7 and 12, our optimized structure for RDX matches well with experimental results, with the average deviation of 1.3% for bond lengths and 0.9% for angles. Few infrared-active intramolecular vibrations are calculated to exist for these molecules in the region studied in this work. For PETN, no intramolecular vibrations are calculated to exist in the region 56–125 cm⁻¹. Clearly, this result indicates that the bulk of the structure seen in the spectra presented here are intermolecular in nature. In this work, although the plane normal of the sample was known accurately, we failed to determine the rotational orientation of the crystals with regard to the incident probe. Our future plans are to perform studies

TABLE 3: Calculated Vibrational Frequencies for RDX, HMX, and PETN in the THz Region

frequency (cm ⁻¹)	IR intensity	Raman activity
RDX ^a		
44	0.0	2.9
58	2.9	0.9
63	1.2	3.3
76	0.0	0.7
HMX ^b		
15	4.3	0.0
51	6.8	0.0
60	0.0	4.3
64	1.4	0.0
66	0.0	2.0
PETN ^c		
24	0.0	2.5
26	2.0	1.3
39	2.0	1.1
40	0.0	2.5
50	0.0	0.7
51	0.0	0.6
56	3.0	2.2

^a This work. ^b Reference 7. ^c Reference 12.

of plane- and rotationally oriented single crystals to determine the direction of the oscillating dipole for the absorption peaks presented here. Additionally, it has been shown that the (110) orientation of PETN is the most sensitive with regard to shock initiation to detonation.¹³ Future studies will attempt to identify absorption peaks for this orientation to elucidate atomic vibrations and perhaps reveal if and how these vibrations relate to shock sensitivity.

Acknowledgment. Crystal growth and sample preparation was supported by the Office of Naval Research. This research was funded in whole or in part by the Intelligence Technology Innovation Center.

References and Notes

- Mittleman, D. *Sensing with Terahertz Radiation*; Springer: New York, 2003.
- Cady, H. H. *Mater. Res. Soc. Symp. Proc.* **1993**, 296, 243.
- Frisch, M. J.; Trucks, G. W.; Schlegel, H. B.; Scuseria, G. E.; Robb, M. A.; Cheeseman, J. R.; Montgomery, J. A., Jr.; Vreven, T.; Kudin, K. N.; Burant, J. C.; Millam, J. M.; Iyengar, S. S.; Tomasi, J.; Barone, V.; Mennucci, B.; Cossi, M.; Scalmani, G.; Rega, N.; Petersson, G. A.; Nakatsuji, H.; Hada, M.; Ehara, M.; Toyota, K.; Fukuda, R.; Hasegawa, J.; Ishida, M.; Nakajima, T.; Honda, Y.; Kitao, O.; Nakai, H.; Klene, M.; Li, X.; Knox, J. E.; Hratchian, H. P.; Cross, J. B.; Adamo, C.; Jaramillo, J.; Gomperts, R.; Stratmann, R. E.; Yazyev, O.; Austin, A. J.; Cammi, R.; Pomelli, C.; Ochterski, J. W.; Ayala, P. Y.; Morokuma, K.; Voth, G. A.; Salvador, P.; Dannenberg, J. J.; Zakrzewski, V. G.; Dapprich, S.; Daniels, A. D.; Strain, M. C.; Farkas, O.; Malick, D. K.; Rabuck, A. D.; Raghavachari, K.; Foresman, J. B.; Ortiz, J. V.; Cui, Q.; Baboul, A. G.; Clifford, S.; Cioslowski, J.; Stefanov, B. B.; Liu, G.; Liashenko, A.; Piskorz, P.; Komaromi, I.; Martin, R. L.; Fox, D. J.; Keith, T.; Al-Laham, M. A.; Peng, C. Y.; Nanayakkara, A.; Challacombe, M.; Gill, P. M. W.; Johnson, B.; Chen, W.; Wong, M. W.; Gonzalez, C.; Pople, J. A. *Gaussian 03*, revision B.04; Gaussian, Inc.: Pittsburgh, PA, 2003.
- Choi, C. S.; Prince, E. *Acta Crystallogr.* **1972**, B28, 2857.
- Cady, H. H.; Larson, A. C. *Acta Crystallogr.* **1975**, B31, 1864.
- Choi, C. S.; Boutin, H. P. *Acta Crystallogr.* **1970**, B26, 1235.
- Brand, H. V.; Rabie, R. L.; Funk, D. J.; Diaz-Acosta, I.; Pulay, P.; Lippert, T. K. *J. Phys. Chem. B* **2002**, 106, 10594.
- Duvillaret, L.; Garet, F.; Coutaz, J. *IEEE J. Sel. Top. Quantum Electron.* **1996**, 2, 739.
- Chen, Y.; Liu, H.; Deng, Y.; Schauki, D.; Fitch, M. J.; Osiander, R.; Dodson, C.; Spicer, J. B.; Shur, M.; Zhang, X. C. *Chem. Phys. Lett.* **2004**, 400, 357.
- Ahn, J.; Efimov, A. V.; Averitt, R. D.; Taylor, A. J. *Opt. Express* **2003**, 11, 2486.
- Gan, C. K.; Sewell, T. D.; Challacomb, M. *Phys. Rev. B* **2004**, 69, 035116.
- Gruzdkov, Y. A.; Gupta, Y. M. *J. Phys. Chem. A* **2001**, 105, 6197.
- Dick, J. J.; Mulford, R. N.; Spencer, W. J.; Pettit, D. R.; Garcia, E.; Shaw, D. C. *J. Appl. Phys.* **1991**, 70, 3572.